Subsynchronous Resonance Mitigation for Series-Compensated DFIG-Based Wind Farm by Using Two-Degree-of-Freedom Control Strategy

Po-Hsu Huang, Mohamed Shawky El Moursi, *Member, IEEE*, Weidong Xiao, *Senior Member, IEEE*, and James L Kirtley, Jr., *Fellow, IEEE*

***Abstract*—This paper investigates a special class of dynamic power system problem, namely subsynchronous resonance (SSR) resulted from a series-compensated network connecting doubly-fed induction generator (DFIG) based wind farms. A novel two-degree-of-freedom (2DOF) control strategy combined with a damping control loop is designed and analyzed for enhancing the system stability and alleviates the SSR that may arise due to the induction generator effect (IGE). The proposed control strategy is tested at different operating conditions of series compensation levels and low wind speeds to ensure the system stability. The doubly-fed induction generator based wind farms without the proposed control strategy leads to overall system instability during high series compensation and low wind speeds. Hence, the mitigation of the SSR and damping enhancement are critical to the entire power system stability. A reliable way of analyzing the system and designing effective control strategies against SSR based on the eigenvalue analysis and impedance based stability criterion is deployed. Moreover, analytical explanations have been elaborated to verify the procedure of the controller design. Fault ride-though capability has also been investigated with the proposed control strategy that is flexible to be integrated with the FRT schemes so as to assist the wind farm in mitigating the SSR during the fault recovery stage. Finally, time domain simulations are carried out to demonstrate the effectiveness of the proposed control strategy for mitigating the SSR and damping power system oscillations.**

***Index Terms*—Doubly-fed induction generator, eigenvalue analysis, series compensated network, subsynchronous resonance, two-degree-of-freedom control.**

NOMENCLATURE

SSR	Subsynchronous resonance.
DFIG	Doubly-fed induction generator.
IGE	Induction generator effect.
2DOF	Two degree of freedom.
GSC	Grid side converter.
RSC	Rotor side converter.
TI	Torsional interaction.
RHP, LHP	Right hand plane, left hand plane.
d, q	Subscript denoting direct and quadrature axes.
R_L, L_L, C_L	Network equivalent resistance, inductance, and capacitance.
$\omega_e, \omega_r, \omega_t$	Nominal grid, rotor, and turbine frequency.
ω_{ssr}	SSR frequency.
v_c, i_c	Series capacitor voltage and current.
v_u, v_s, v_r	Grid, stator, and rotor voltage.
C_p	Coefficient of performance of the blade.
V_w	Wind speed.
$\theta_{sh}, T_{sh}, K_{sh}$	Shaft angle, torque, and stiffness.
H_t, H_g	Turbine and generator inertia.
T_t, T_e	Turbine and electrical torque.
D_{mutual}	Mutual damping of drivetrain system
i_s, i_r, i_g	Stator, rotor, and GSC current.
R_s, R_r	Stator and rotor resistance.
Q_g	Generator reactive power.
K_{p1}, K_{i1}	PI gains of the RSC's torque controller.
K_2, K_{i2}	PI gains of the RSC's reactive power controller.
K_{p3}, K_{i3}	PI gains of the RSC's current controller.
K_{p4}, K_{i4}	PI gains of the GSC's DC-link controller.
K_{p5}, K_{i5}	PI gains of the GSC's voltage controller.
K_{p6}, K_{i6}	PI gains of the GSC's current controller.
L_g, R_g	Filter line inductance and resistance.
V_{dc}, C_{dc}	DC-link voltage and capacitance.
P_{rsc}, P_{gsc}	RSC and GSC active power.
Δv_c	Damping signal for the GSC.
K_d	Derivative gain of the 2DOF controller.

Manuscript received February 05, 2014; revised June 04, 2014 and July 16, 2014; accepted August 09, 2014. Paper no. TPWRS-00170-2014.

P.-H. Huang, M. S. El Moursi, and W. Xiao are with the iEnergy Center and the Electrical Engineering and Computer Science Department, Masdar Institute of Science and Technology, Abu Dhabi, UAE (e-mail: melmoursi@masdar.ac.ae).

J. L. Kirtley, Jr. is with the Department of Electrical Engineering and Computer Science, the Massachusetts Institute of Technology, Cambridge, MA 02139 USA.

Color versions of one or more of the figures in this paper are available online at http://ieeexplore.ieee.org.

Digital Object Identifier 10.1109/TPWRS.2014.2348175

I. Introduction

SUBSYNCHRONOUS resonance (SSR) is an electric power system condition in which the electric network exchanges energy with a turbine generator at the one or more natural frequencies below the synchronous frequency [1]. It occurs when the series-compensated network is connected to a power system. Due to its significant impact, the SSR phenomenon has been observed and investigated with conventional power plants [2]–[7]. The increased penetration of wind power generation has recently drastically affected system dynamics. For the large scale wind farms connected through long transmission lines, the series compensation is commonly used to maintain the power transfer capability, minimize the transmission line reactance and line voltage drop, reduce the transmission angle, and increase the system stability [8]. However, it adds the drawback of SSR phenomena with induction generators. Thus, a growing emphasis has been laid on the study of the induction generator based wind turbines connected to a series-compensated network [9], [10]. The capability of flexible AC transmission devices (FACTs) has been demonstrated with its effectiveness in mitigating SSR for induction generators. In [11], an advanced control for thyristor controlled series capacitors (TCSC) is proposed to alleviate the SSR; a damping controller with static synchronous compensators (STATCOM) has been developed in stabilizing a series-compensated wind farm [9].

Among all the wind turbine technologies, doubly-fed induction generators (DFIGs) with variable speed operation are widely being used today. The adoption of DFIGs is booming for many reasons such as mechanical stress reduction, acoustic noise mitigation, and the flexibility of active and reactive power control based on back-to-back converters between the grid and the induction machine rotor circuit. Consequently, the complexity increases and the system becomes difficult to analyze without a systematic point of view. Hence, many studies have been proposed by using eigenvalue analysis with a linearization technique to evaluate the transient dynamics of power electronics integrated systems. This approach has the following advantages [4]: 1) one-time computation for all the system modes; 2) it is convenient to investigate parameter variation of the system; 3) analytical methods such as root locus and eigenvalue movement can be utilized to provide an accurate analysis. Thus, a comprehensive study for modeling of DFIG-based wind farms based on the eigenvalue analysis has been addressed to show the system behavior of the wind turbines with a series-compensated network [12]. The investigation presents the potential of applying the eigenvalue analysis to the system of high complexity. Two of the SSR phenomena have been addressed, showing induction generator effect (IGE) due to the negative resistance at SSR frequency and torsional interaction (TI) from energy exchange between the turbine and LC network. The advantage has been shown that the eigenvalue extraction technique offers a clear picture of the system to design a better control strategy. The authors also continued the work with more detailed explanation to investigate the potential solution for the DFIG to handle the SSR phenomena.

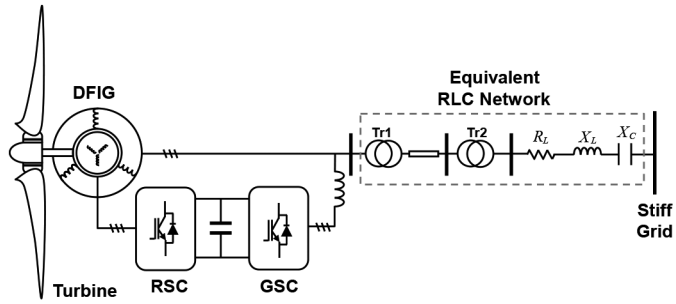

Fig. 1. System diagram for an aggregated DFIG-based wind farm connected to a series-compensated network.

A DFIG suffers specially from the IGE in subsynchronous speed operation since a larger negative resistance caused by the low rotor speed tends to degrade system damping and stability. The system becomes unstable and highly oscillatory when the compensation level is high. The supplementary damping control loop by using shunt connected voltage source converters (VSCs) has been widely applied in damping power system oscillation [9], [13], [14]. By utilizing the same function as the shunt connected VSCs, an SSR damping voltage control loop by using the grid side converter (GSC) is proposed with a detailed analysis to mitigate the oscillation [15]. However, the damping performance is directly affected by the controller's practical limitations and the GSC's partial rating. A further investigation on different operating points and converter's rating is necessary to achieve a reliable solution. Meanwhile, the rotor side converter (RSC) directly regulates the generator's active and reactive power, which is higher than the GSC's rating. This indicates a potential of utilizing the RSC to assist in damping the SSR of the system. Notably, the RSC controller has impacted the system stability due to the equivalent dynamic behavior of negative resistance. Alternative control strategies should be applied to improve the dynamic response with properly selected controller gains.

This paper introduces a new control strategy with a two-degree-of-freedom (2DOF) configuration by utilizing the RSC's current control loop to mitigate the SSR for the DFIG based wind turbines. To achieve such an objective, the eigenvalue analysis with the linearized system is studied to provide a systematic evaluation of the system status against the nonlinear feature. The system modeling is first illustrated in Section II, followed by the model evaluation based on the eigenvalue analysis presented in Section III. Section IV demonstrates the structure of the proposed 2DOF controller as well as the combined mitigation strategy and investigates their influence on the system stability through both the impedance based criterion and eigenvalue analysis. Finally, a necessary time-domain analysis is shown in Section V to verify the proposed mitigation strategies; the conclusion is drawn in Section VI.

II. System Modeling

Fig. 1 illustrates the system diagram that is investigated in this study. It includes a DFIG based wind farm connected to the infinite bus through two step-up transformers and transmission lines. The wind farm is rated at 400 MVA in aggregated capacity

TABLE I
SYSTEM PARAMETERS

Generator Data		Converter Data	
Aggregated Rating	1.67MVA*240	Coupling inductor	0.3 pu
Rated voltage	575 V	Coupling resistor	0.02 pu
Rated frequency	60 Hz	Dc-link voltage	1200 V
Stator resistance	0.0023 pu	Dc-link capacitor	14 mF
Stator inductance	0.18 pu	Drivetrain Data	
Mutual inductance	2.9 pu	Mutual damping	1.5 pu/pu
Rotor resistance	0.016 pu	Shaft stiffness	1.11 pu/rad
Rotor inductance	0.16 pu	Turbine Data	
Inertia H_g	0.685 s	Inertia H_t	4.32 s
Tr1 575V/25kV		Scaled Grid	
Aggregated Rating	1.83MVA*240	X_L	0.4 pu
Leakage inductance	0.07 pu	R_L	0.02 pu
Tr2 25kV/120kV		X_C	0-0.3pu
Aggregated Rating	440MVA*2	Frequency	60Hz
Leakage inductance	0.08 pu	Base power	400MVA

(the models are derived based on p.u. system and suitable for different scales of the system). The wind turbine and converter parameters are referred to the GE® 1.5-MW wind turbine [16]. The impedance of the equivalent RLC network is 0.5 pu with the base power of 400 MVA. The series capacitance varies from 0 to 0.3 pu (60%), and the resistance is 0.02 pu. The parameters are shown in Table I. To obtain a linearized state-space system, the models are derived in dq reference frame and the power electronic converters are replaced by controllable voltage sources.

A. Grid and Compensation Network Model

The RLC network model characterizes both equivalent impedance and series capacitor. The resonance features are captured in the representation of synchronized rotating frame through park's transformation and can be observed with the frequency components of $\omega_{ssr}-\omega_e$ and $\omega_{ssr}+\omega_e$. The model is implemented by

$$\begin{aligned} pv_{cd} &= \omega_e v_{cq} + \frac{i_{cd}}{C_L} \\ pv_{cq} &= -\omega_e v_{cd} + \frac{i_{cq}}{C_L} \\ pi_{cd} &= \frac{-v_{cd}}{L_L} - (\frac{R_L}{L_L})i_{cd} - \omega i_{cq} + \frac{(v_{ud}-v_{sd})}{L_L} \\ pi_{cq} &= \frac{-v_{cq}}{L_L} + \omega_e i_{cd} - (\frac{R_L}{L_L})i_{cq} + \frac{(v_{uq}-v_{sq})}{L_L} \end{aligned} \tag{1}$$

where $p = d/dt$.

B. Turbine and Drive Train

The p.u. turbine model is expressed as

$$T_t = \frac{K_1 C_p V_w^3}{\omega_t} \tag{2}$$

where K_1 is the coefficient of the equation. In addition, two-mass drive train model is utilized in the simulation, which can be shown as

$$\begin{aligned} p\theta_{sh} &= (\omega_t - \omega_r) \\ p\omega_t &= \frac{(T_t - T_{sh})}{2H_t} \\ p\omega_r &= \frac{(T_{sh} - T_e)}{2H_g} \\ T_{sh} &= K_{sh}\omega_e\theta_{sh} + D_{mutual}p\theta_{sh}. \end{aligned} \tag{3}$$

C. DFIG Model

The mathematical models for DFIGs are commonly expressed in (4) with reference to the dq reference frames:

$$\begin{cases} v_{sd} = R_s i_{sd} - \omega_e\psi_{sq} + p\psi_{sd} \\ v_{sq} = R_s i_{sq} + \omega_e\psi_{sd} + p\psi_{sq} \\ v_{rd} = R_r i_{rd} - (\omega_e - \omega_r)\psi_{rq} + p\psi_{rd} \\ v_{rq} = R_r i_{rq} + (\omega_e - \omega_r)\psi_{rd} + p\psi_{rq} \end{cases} \tag{4}$$

where ψ_{sd} and ψ_{sq} indicates the stator flux linkage, ψ_{sd} and ψ_{rq} are the rotor flux linkage.

D. Rotor Side and Grid Side Converters

The DFIG's back-to-back converter behaves like a controlled voltage source and directly regulates the output current. The RSC outer loop controllers are shown as follows:

$$\begin{aligned} i_{rd}^* &= (\frac{K_{p1}+K_{i1}}{s})(T_e - T_e^*) \\ i_{rq}^* &= (\frac{K_{p2}+K_{i2}}{s})(Q_g - Q_g^*) \end{aligned} \tag{5}$$

where * denotes the desired reference. Moreover, The RSC inner current controllers can be described as

$$\begin{aligned} v_{rd} &= (\frac{K_{p3}+K_{i3}}{s})(i_{rd}^* - i_{rd}) + \delta_{rd} \\ v_{rq} &= (\frac{K_{p3}+K_{i3}}{s})(i_{rq}^* - i_{rq}) + \delta_{rq} \end{aligned} \tag{6}$$

where δ_{rd} and δ_{rq} are feed-forward terms. Similarly, the control of GSC has both outer dc-link and stator voltage regulators, which can be expressed as

$$\begin{aligned} i_{gd}^* &= (\frac{K_{p4}+K_{i4}}{s})(V_{dc} - V_{dc}^*) \\ i_{gq}^* &= (\frac{K_{p5}+K_{i5}}{s})(V_s^* - V_s). \end{aligned} \tag{7}$$

The inner control loop of the GSC can be also displayed as

$$\begin{aligned} v_{gd} &= (\frac{K_{p6}+K_{i6}}{s})(i_{gd}^* - i_{gd}) + \delta_{gd} \\ v_{gq} &= (\frac{K_{p6}+K_{i6}}{s})(i_{gq}^* - i_{gq}) + \delta_{gq} \end{aligned} \tag{8}$$

where δ_{gd} and δ_{gq} are feed-forward terms. The grid side converter output filter is represented as

$$\begin{aligned} pi_{gd} &= -(\frac{R_g}{L_g})i_{gd} + \omega_e i_{gq} + \frac{(v_{gd}-v_{sd})}{L_g} \\ pi_{gq} &= -(\frac{R_g}{L_g})i_{gq} - \omega_e i_{gd} + \frac{(v_{gq}-v_{sq})}{L_g}. \end{aligned} \tag{9}$$

The dc-link is derived as a first order model to show the capacitor dynamics:

$$
\begin{aligned}
V_{dc}C_{dc}pV_{dc} &= P_{rsc} - P_{gsc} \\
P_{rsc} &= v_{rd}i_{rd} + v_{rq}i_{rq} \\
P_{gsc} &= v_{gd}i_{gd} + v_{gq}i_{gq}.
\end{aligned} \tag{10}
$$

III. Model Evaluation

To integrate the above-mentioned equations, an external constraint equation should be formed to link the DFIG model to the RLC network, as shown in Fig. 1. In both DFIG and network models, the terminal voltages are considered as system input variables. The relation between the models can be built by ignoring the dynamic of the GSC filter. Therefore, the GSC filter is configured as a link to generate the stator voltage from the filter current and converter output voltage [12]. Another approach in [17] applies the equations of active and reactive power exchange; however, the network dynamics will be ignored. To preserve the dynamic behavior of both the network and GSC output filter, an extra constraint is introduced by connecting the stator, GSC filter output, and RLC network to the same terminal. To facilitate the process, a simple way can be utilized by connecting the common terminal to a large resistance $(1\text{e}4 \sim 1\text{e}7\ \text{pu})$ to obtain a semi-explicit differential algebraic equation (DAE):

$$
\begin{aligned}
\dot{X} &= (X, Z, U) \\
0 &= g(X, Z, U)
\end{aligned} \tag{11}
$$

where X and Z are the differential and algebraic variables, and U is the system input. It should be also mentioned that the variation of the resistance within this range should not induce noticeable deviations of the system modes. To snap shot the small-signal dynamic responses of the system, first-order linearization can be used to obtain

$$
\dot{\tilde{X}} = \tilde{A}\tilde{X} + \tilde{B}\tilde{U}\,\big|_{X_0, Z_0, U_0} \tag{12}
$$

where

$$
\begin{aligned}
\tilde{A} &= \frac{\partial f}{\partial X} - \frac{\partial f}{\partial Z}\left(\frac{\partial g}{\partial Z}\right)^{-1}\frac{\partial g}{\partial X} \\
\tilde{B} &= \frac{\partial f}{\partial X} - \frac{\partial f}{\partial Z}\left(\frac{\partial g}{\partial Z}\right)^{-1}\frac{\partial g}{\partial X}.
\end{aligned} \tag{13}
$$

With the linearized system based on state-space representation, the eigenvalues can reveal the system modes around the operation points.

By extracting the eigenvalues of $\tilde{A}$, four dominant modes are obtained, as shown in Table II. The operating conditions are given as: wind speed of 11m/s, rotor speed of 1.2 pu, and compensation level of 25% $(X_c = 0.25X_L)$. Since the frequency of the resonant components become $\omega_e + \omega_{ssr}$ and $\omega_e - \omega_{ssr}$ in the rotating synchronized reference frame, $\lambda_{1,2}$ represents the supersynchronous mode and $\lambda_{3,4}$ stands for the subsynchronous modes. Moreover, $\lambda_{5,6}$ can be identified as an electromechanical (EM) mode, which is impacted by both DFIG circuits and mechanical dynamics. In addition, the state-to-mode participation factors are given in Table III based on various operating conditions. Although the participation factor shows no direct link between the mechanical variables to the EM mode as relatively large time constants of the mechanical system, it can still be observed that the variation of the wind speed and its corresponding change of rotor speed affect its oscillation frequency, which is directly linked to the rotor slip frequency due to the existence of the complimentary frequency component in the rotor windings. Finally, the participation factors show that $\lambda_{7,8}$ is affected mostly by the mechanical variables.

TABLE II
System Modes at Wind Speed of 11m/s With 25% Series Compensation

	Eigenvalues	Mode
$\lambda_{1,2}$	-11.68±526.25i	Supersynchronous Mode
$\lambda_{3,4}$	-5.58±231.73i	Subsynchronous Mode
$\lambda_{5,6}$	-11.79±35.7i	Electromechnical (EM) Mode
$\lambda_{7,8}$	-0.68±18.86i	Torsional Mode

TABLE III
Participation Factor (State-to-Mode) and Eigenvalues of System Modes at Different Operating Conditions

Mode	SSR	Torsional	EM	SSR	Torsional	EM
Level	40%			60%		
Speed	6m/s, ω_r= 0.7 pu					
σ	**7.83**	-0.65	-36.1	**38.4**	-0.66	-66.4
$\pm\omega i$	±175.1i	±18.82i	±101.9i	±135.67	±18.82i	±102.9i
i_{sdq}	**.4565**	0	**.4473**	**.4555**	0	**.4500**
i_{rdq}	**.4726**	0	**.5195**	**.4851**	0	**.5074**
ω_r	0	**.4311**	0	0	**.4311**	0
θ_{sh}	0	**.4978**	0	0	**.4979**	0
ω_t	0	.0679	0	0	.0680	0
Speed	9m/s, ω_r= 0.98 pu					
σ	-3.92	-0.61	-13.4	-0.47	-0.63	-16.56
$\pm\omega i$	±191.5i	±18.87i	±7.948i	±149.5i	±18.86i	±8.252i
i_{sdq}	**.4598**	.0015	**.4307**	**.4671**	.0139	**.4422**
i_{rdq}	**.4351**	.0017	**.5278**	**.4484**	.0159	**.5253**
ω_r	**0**	**.4188**	0	0	**.4199**	0
θ_{sh}	**0**	**.4808**	0	0	**.4826**	0
ω_t	**0**	.0654	0	0	.0657	0
Speed	11m/s, ω_r= 1.2 pu					
σ	-3.94	-0.68	-12.8	-1.79	-0.68	-14.3
$\pm\omega i$	±194.6i	±18.85i	±39.58i	±156.5i	±18.85i	±44.44i
i_{sdq}	**.4292**	.0109	**.4368**	**.4685**	.0086	**.4419**
i_{rdq}	**.4199**	.0145	**.5435**	**.4285**	.0110	**.5372**
ω_r	0	**.4216**	0	0	**.4239**	0
θ_{sh}	0	**.4844**	0	0	**.4876**	0
ω_t	0	.0659	0	0	.0664	0

A. Impact of IGE and Torsional Modes

Since the SSR slip is usually smaller than zero as $\omega_{ssr} < \omega_r$, the rotor equivalent resistance, R_r/s_{ssr}, behaves like a negative resistance as seen from the stator terminals. When the total network resistance is negative, the instability occurs at the SSR frequency. This phenomenon is called IGE. The self-sustained oscillation occurs when the total network resistance becomes negative. The observation is made by changing the compensation level and wind speed, shown in Table III. It can be seen that

at the same compensation level the higher the wind speed generally results in the better the SSR damping. The reason is because the increase of the rotor speed causes the subsynchronous slip, $s_{ssr} = (\omega_{ssr} - \omega_r)/\omega_{ssr}$, to have a larger negative value, introducing a smaller negative rotor equivalent resistance. Similarly, a higher compensation level attributes to a larger negative rotor equivalent resistance. The above phenomena have also been identified in [13].

In addition, the wind turbines usually have a relatively lower shaft stiffness (e.g., 1.1 pu/rads in this case) with its low power rating. In Table II, the torsional mode is around 3 Hz and increasing the shaft stiffness results in a higher torsional resonance frequency. In this paper, the torsional mode is not directly affected by the compensation level since the complementary SSR frequency at 60% compensation is still far higher than the torsional mode, indicating the absence of the torsional amplification.

B. Impact of RSC and GSC Controller

The impact of the controller gains of RSC and GSC is shown by the eigenvalue loci of the SSR mode in Fig. 2. It can be found out that by increasing the RSC controller P gain, K_{p3}, the SSR mode moves toward RHP. The same effect can be observed through the P gains, K_{p1}, K_{p2}, of the RSC outer torque and reactive power loops. To simplify the derivation, the d-axis rotor voltage is utilized to show the small-signal dynamic equation in response to the d-axis rotor current, shown in (14):

$$\begin{aligned}\tilde{v}_{rd} &= K_{p3}\tilde{i}^{*}_{rd} - K_{p3}\tilde{i}_{rd} = K_{p1}K_{p3}\tilde{T}_e - K_{p3}\tilde{i}_{rd} \\ &= K_{p1}K_{p3}(-\lambda_{dm}\tilde{i}_{rq} + \lambda_{dm}\tilde{i}_{rq}) - K_{p3}\tilde{i}_{rd} \\ &= -K_{p3}(K_{p1}\lambda_{dm} + 1)\tilde{i}_{rd} + K_{p1}K_{p3}\lambda_{qm}\tilde{i}_{rq}. \quad (14)\end{aligned}$$

By neglecting the coupling term $\tilde{i}_{rq}$, the rotor dynamic resistance can be obtained:

$$R_{dynamic} = \frac{(\frac{\tilde{v}_{rd}}{s_{ssr}})}{-\tilde{i}_{rd}} = -\frac{K_{p3}(K_{p1}\lambda_{dm} + 1)}{|s_{ssr}|}. \quad (15)$$

It should be noticed that rotor terminal voltage is divided by s_{aar} in SSR reference frame. Since the SSR slip s_{aar} is negative, increasing K_{p1} and K_{p3} will necessarily make the dynamic resistance more negative, showing poorer damping of the SSR mode. The impact from the controller parameter variation is summarized in Table IV.

IV. SSR Mitigation Strategy

The IGE and controller parameters show impacts on the SSR mode which can cause instability of the system. Table III indicates that the SSR mode is poorly damped when the compensation level is high. Thus, the ideal damping controller is required to operate the DFIG wind farm at high compensation levels. In conventional approaches, the damping controller has been implemented with a STACOM to provide auxiliary damping control to series-compensated self-excited induction generator (SEIG) based wind farms. Rotor speed and generator power are chosen as damping signals to improve the system dynamic response. Furthermore, the SSR damping control loop with both DC-link and terminal voltage control loops by using the GSC

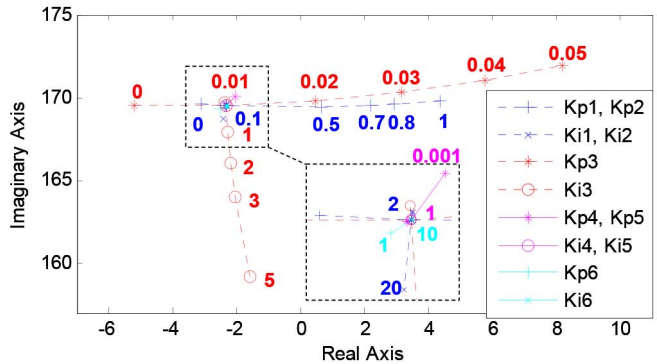

Fig. 2. Eigenvalue loci of the SSR mode in variation to controller gains (base case parameters: 50% compensation, 9 m/s wind speed, Kp1, Kp2 = 0.1, Ki1, Ki2 = 2, Kp3 = 0.01, Ki3 = 0.1, Kp4 = 0.2, Ki4 = 0.4, Kp5 = 0.01, Ki5 = 0.04, Kp6 = 4, Ki6 = 100).

TABLE IV
IMPACT OF THE CONTROLLER GAINS TO THE SSR MODE

Controller Parameter	Frequency	Damping
RSC outer loop P gains (K_{p1}, K_{p2})	**increases**	**decreases**
RSC outer loop I gains (K_{i1}, K_{i2})	decreases	slightly increases
RSC current loop P gain (K_{p3})	**increases**	**significantly decreases**
RSC current loop I gain (K_{i3})	decreases	slightly decreases
GSC outer loop P gains (K_{p4}, K_{p5})	decreases	almost no impact
GSC outer loop I gains (K_{i1}, K_{i2})	no impact	no impact
GSC current loop P gain (K_{p3})	increases	almost no impact
GSC current loop I gain (K_{i3})	no impact	no impact

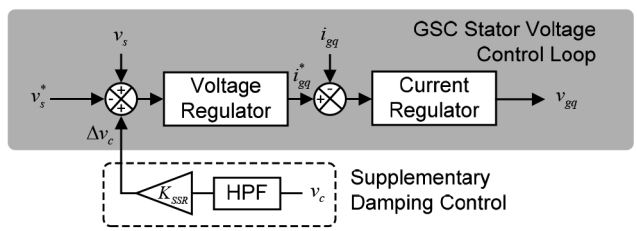

Fig. 3. Damping control loop with the GSC stator voltage controller.

has been demonstrated with its effectiveness in stabilizing the system. The diagram of the applied damping controller is shown in Fig. 3 by using the series capacitor voltage as the damping signal. Also, a high-pass filter (HPF) is utilized to avoid interfering system normal operation. The cut-off frequency is chosen as 10 HZ to preserve the SSR component and to remove the DC value so as not to disturb the steady-state operation. For the damping control signals, many other system variables are also available, while their detrimental effects on other system modes may induce instability of the system. The recognition of using the capacitor voltage as the damping signal has been addressed in [15].

The major limitation of the supplementary damping controller is the restricted voltage control capability of the shunt-connected GSC. Especially, in the case with the high compensation level and the low wind speed, a necessary high damping gain is required. This can be seen from the root locus plot in Fig. 4, which shows that to achieve the damping ratio of 5% the gain should be selected as high as 990. This implies that using solely the GSC to stabilize the system with large series

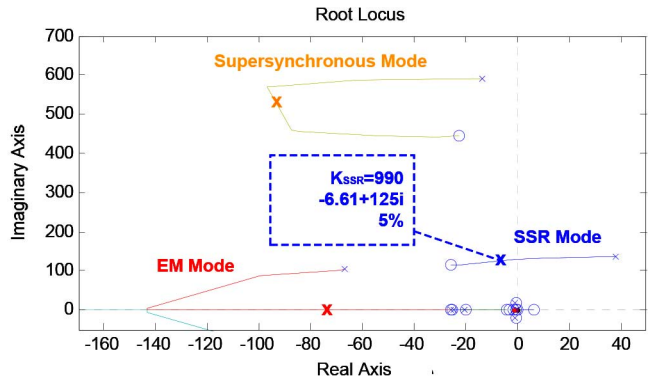

Fig. 4. Root locus of the system modes in respect to the varying KSSR with the damping signal selected as the series capacitor voltage vc. (60% compensation, 6 m/s wind speed).

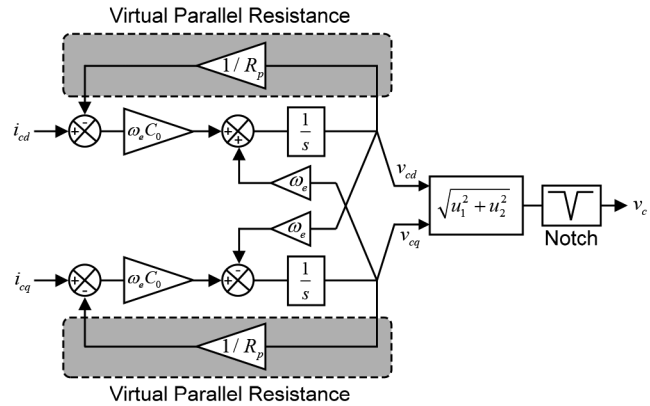

Fig. 5. Proposed capacitor voltage estimation method.

capacitance might be insufficient. Thus, approaches to handle the severe cases are to be discussed in order to ensure the system stability throughout the possible operating conditions.

A. Improved Capacitor Voltage Estimation Method

As presented in the previous section, the capacitor voltage shows direct improvement in damping the SSR mode. In practice, however, measuring capacitor voltage requires long-distance and high-bandwidth commination, causing significant overall cost to the system installation. Therefore, estimation of the capacitor voltage seems like a preferred solution as transmission line current can be measured from the wind farm terminal. Although directly using the line current for the damping control loop may help in the SSR mode, detrimental impacts on the other modes are likely to be induced, as mentioned earlier. To ensure the system overall stability, capacitor voltage estimation is necessary. In [15], it has been proposed that the capacitor voltage magnitudes can be estimated through each phase by the simple realization of integrating the line currents:

$$v_{a,b,c} = \frac{1}{C}\int i_{a,b,c}\, dt \tag{16}$$

where a, b, c denote instantaneous signals. In this case, the line current can then be measured at the wind park terminal. Although the series capacitance is unknown, it has only determined the magnitude of the resonance, and the resonance frequency is still preserved with the estimated signal. Thus, the selection of the damping control gain and assumed compensation level can be based on the severe-case scenarios to allow proper functionality during high compensation cases. To avoid DC offsets being preserved into the predicted voltage signal, the integration should take place when the current reaches zero so that resonance at the nominal frequency does not appear in the damping signal Δv_c (DC offset oscillates at nominal frequency as seen from the synchronous reference frame). However, sudden change of the capacitor steps or faults may bring the DC offset back; this synchronous oscillation in the damping signal is not likely to be mitigated since the main purpose of the damping control loop is to preserve the bandwidth around the SSR frequency. Using the low-pass filter causes a significant phase shift and therefore fails the damping function. A notch filter is good for suppressing the oscillation, while the sustained resonance cannot be removed completely and will affect the GSC's voltage control loop even during the steady state.

To solve this issue, an improved estimation method is proposed based on the synchronous reference frame with the estimation model shown in Fig. 5. It can be seen that a virtual resistor is implemented in order to damp the fundamental oscillation. The virtual resistance should be relatively larger than the nominal impedance of the series capacitor to give reasonable rate of decay without affecting the voltage dynamics. The comparison of the Δv_c between the cases with and without the proposed method is shown in Fig. 6. In this comparison, $\omega_e C_0$ *and* R_p are assumed to be 0.125 pu (25% of grid reactance 0.5) and 3 pu; the notch filter is centered at 60 Hz with the damping coefficient of 0.1; the compensation level changes from 25% to 40% at 0.2 s. It can be observed that the dynamic behavior of Δv_c with the proposed method matches closely with the actual case, while without the proposed method significant oscillation at fundamental frequency appears due to the DC components. It is mentioned previously that damping gain can be selected based on the severe-case scenario (highest possible compensation levels). If the actual compensation level is larger than the assumed, the estimated magnitude will be lower than the actual measurement. To ensure proper magnitude of Δv_c, the maximum compensation level is recommended to be chosen; in this case, the damping performance in high-compensation cases can be ensured, while in low-compensation levels the SSR is much less harmful so that the magnitude difference has no direct influences on the system stability. The detailed evaluation will be carried out in the later session.

B. Concept of 2DOF Control Strategy

The concept of 2DOF control strategy is introduced in this study, which comprises of derivative controllers connected to the current control loop of the RSC. A 2DOF PID control structure shows flexibility to achieve an improved control performance compared to traditional one degree of freedom (1DOF) PID control, which has been reported in [18]. Fig. 7 shows the control diagram illustrating the concept of 2DOF derivative controllers. It can be seen that the current reference signal is removed from the derivative controller so that only the actual current signal pass through the K_d term. This means that the pro-

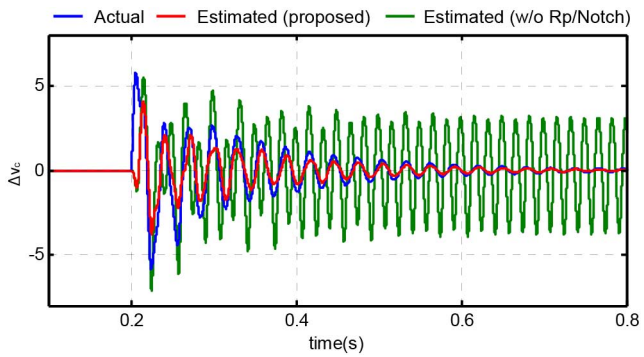

Fig. 6. Comparison of damping signal between different cases (compensation level changes from 25% to 40% at 0.2 s).

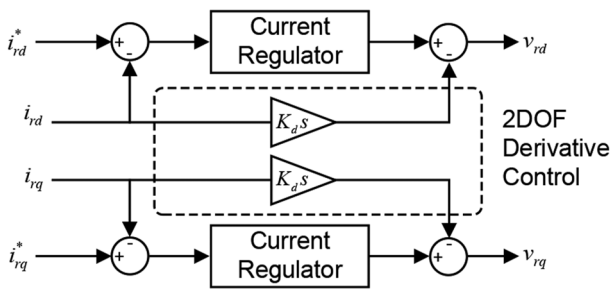

Fig. 7. 2DOF derivative control with the RSC current loop.

posed strategy aims to enhance the system stability against the SSR and follows the typical PID controller design so as to ensure the practicality of the control structure for the current control loop. It should be noticed that for general 2DOF approaches with the derivative controller, the objective is to achieve harmless zero cancellations by separating the set-point response from the disturbance rejection, while in this paper the aim is to ensure that the dynamics of the external controllers' output (torque/reactive power controllers) do not affect the derivative actions by removing the current reference from the derivative term input.

The impact of the derivative action can then be investigated through the impedance based stability criterion [19], [20]. First, the relation of the rotor terminal voltage to the rotor current can be derived as $\tilde{V} \cong (d/dt)K_d(-\tilde{I}_r)$. A negative sign is added to show the perspective from the stator terminal, by which the dynamic behavior of rotor voltage resembles a virtual inductance. Fig. 8 shows the small-signal equivalent circuit of the DFIG system connected to the grid. It should be noticed that the derivative action is modeled as a virtual inductance connected in series with the rotor circuit. In this case, both the GSC and RSC's current controllers are assumed to be disabled in order to bring the attention to the impact of the derivative control; thus, only the derivative controller responds to the system disturbances. By neglecting the shunt connected GSC and mutual inductance, the relation between grid voltage and line current, $I(s) = G(s)V(s)$, can be obtained:

$$G(s) = \frac{1}{(Z_{NET}(s) + Z_{DFIG}(s))} \tag{17}$$

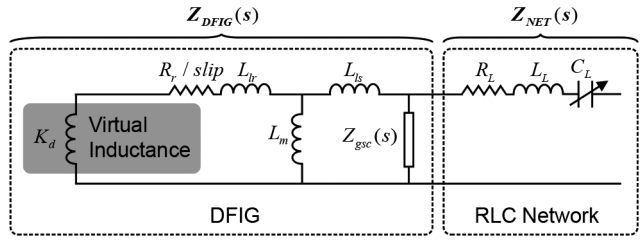

Fig. 8. Equivalent circuit of the DFIG connected to the series-compensated network.

where

$$Z_{NET}(s) = \frac{1}{sC_L + sL_L + R_L}$$
$$Z_{DFIG}(s) = R_s + s(L_{ls} + L_{lr} + Kd) + \frac{R_r}{slip}$$

where $slip = (s - j\omega_r)/s$. The poles of $G(s)$ can be used to reveal the dynamic characteristic of the system. To investigate the impact of the K_d, (17) can be represented by

$$G(s) = \frac{\frac{s}{L_{eq}}}{s^2 + s(\frac{R_{eq}}{L_{eq}}) + \frac{1}{L_{eq}C_L}} \tag{18}$$

where $L_{eq} = L_L + L_{ls} + L_{lr} + K_d$ and $R_{eq} = R_L + R_s + R_r(\omega)$. It can been seen that when $\omega \rightarrow \omega_{ssr}$ and $R_r(\omega_{ssr}) < -(R_L + R_s)$, the system becomes unstable due to unstable poles. This agrees with the phenomenon of the IGE that self-sustained oscillations occur when the total network resistance becomes negative. From (18), the impact of the K_d can be classified into two criteria:

1) Increase of K_d leads to a larger L_{eq}, resulting in lower SSR frequency (lower natural frequency) and less negative $R_r(\omega_{ssr})$.
2) If R_{eq} is positive enough, the increase of L_{eq} reduces the magnitude of first order term in the denominator and moves the SSR pole to RHP.

The bode diagram of the $G(s)$ in respect to variation of K_d from 0 to 0.001 is shown in Fig. 9. The rotor speed is 0.7 p.u. (6m/s) and the compensation level is 60%. It can be observed that the derivative action helps to reduce the SSR frequency, which is very helpful in mitigating the IGE that tends to induce negative total resistance in high compensation levels. To verify the small-signal impedance-based analysis, the SSR pole movement of $G(s)$ in response to a varying K_d gain is compared to the eigenvalue locus of the SSR mode in compensation levels of 60% and 25%, as shown in Fig. 10. The eigenvalue extraction is based on the case in which the shunt connected GSC and the RSC controller are disabled. In Fig. 10(a), both the SSR pole and eigenvalue move toward LHP as the reduced resonance frequency induces a less negative R_{eq}, identifying the criterion 1). In Fig. 10(b), the movement toward RHP indicates existence of relatively large R_{eq}, which can be illustrated by criterion 2).

The relationship of the total equivalent resistance and real part of the SSR mode (through the eigenvalue analysis) versus compensation level is plotted in Fig. 11(a). Some observations can be obtained:

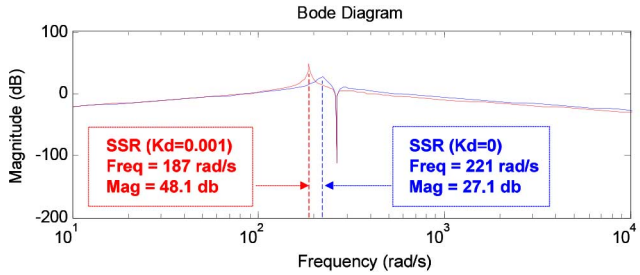

Fig. 9. Bode diagram of G(s). (60% compensation, 6 m/s wind speed).

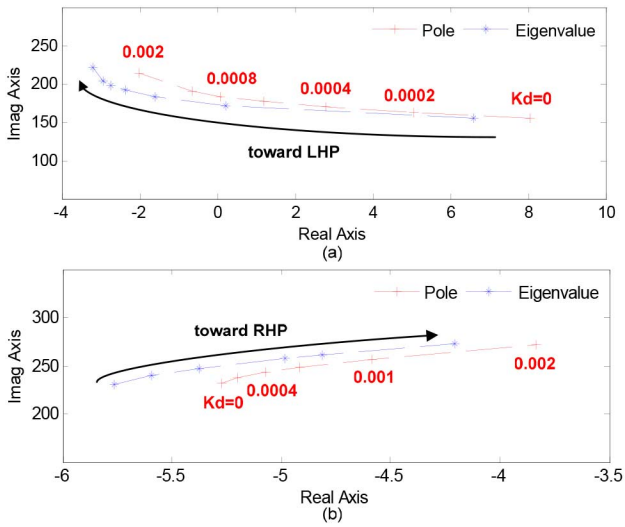

Fig. 10. Verification of the impedance based analysis by comparing the pole movement and eigenvalue locus with increasing K_d (complementary frequency representation $\omega_e - \omega_{ssr}$). (a) 60% compensation, 6 m/s wind speed. (b) 25% compensation, 6 m/s wind speed. (Simplified model: The current controllers of GSC and RSC are disabled with only the derivative controller enabled.)

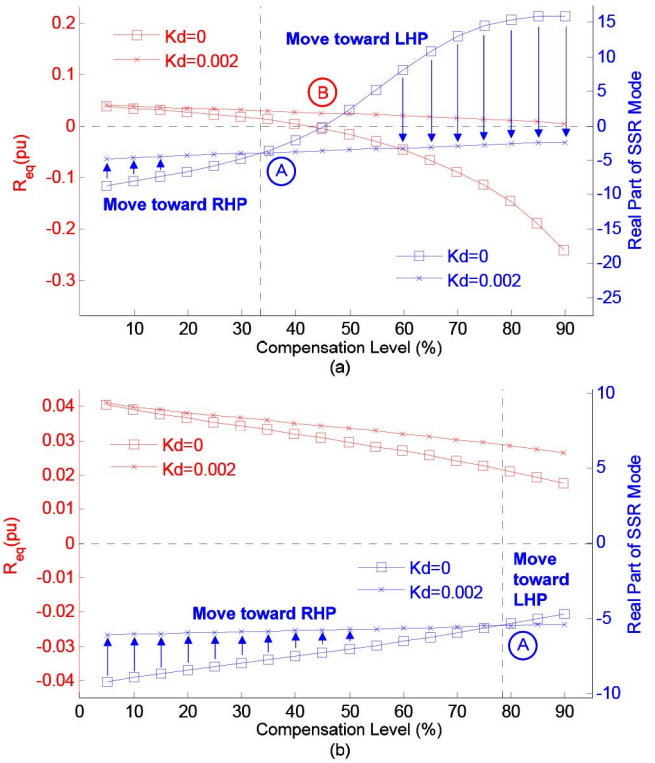

Fig. 11. Red: Equivalent total resistance versus compensation level. Blue: Real part of SSR mode versus compensation level. (a) rotor speed $= 0.7$ pu, wind speed $= 6$ m/s. (b) rotor speed $= 1.2$ pu, wind speed $= 11$ m/s. (Simplified model: The current controllers of GSC and RSC are disabled with only the derivative controller enabled.)

1) When the compensation level below 33% (A point), the K_d gain moves the SSR mode toward RHP; above 33%, the SSR mode moves toward LHP.
2) When $R_{eq} < 0$ (B point), the real part of the SSR mode becomes positive, causing instability to the system.
3) The derivative action maintains a positive value of R_{eq} and keeps the SSR mode in the LHP over the range of the compensation level.

Therefore, it is shown that the derivative controller significantly improve the system stability during high compensation levels. Moreover, another case study based on the wind speed of 11m/s is shown in Fig. 11(b). It can be seen that the critical point (A point), at which the direction of the SSR mode movement changes, becomes much higher compared to the case in low wind speed (33% to 77%). This is because at high rotor speeds the R_{eq} remains relative large and positive [criterion 2)] so that the effect of the derivative action in improving the stability cannot be seen until a very high compensation level. Although the derivative action may shift the SSR mode toward RHP, the real part of the mode remains relatively negative (around -6). Thus, the system remains stable.

To sum up, the impedance-based stability analysis provides an easy-to-view mathematical explanation showing the impact of the proposed 2DOF control strategy on the SSR mode. A virtual impedance helps to mitigate the stability issue caused by the SSR at the high compensation levels and low wind speeds. The eigenvalue analysis based on the simplified model with only the derivative control is then utilized to verify the impedance-based stability theory in order to show the efficacy of the analytical analysis.

C. Combined Damping and 2DOF Control Strategy

The proposed 2DOF control is to improve the rotor dynamic response and mitigate the IGE in the high compensation level. In this case, while the derivative term improves the SSR damping significantly, a larger K_d gain might bring other system modes into instability, e.g., the electromechanical mode. Also, at low compensation levels the SSR mode may become less damped. Therefore, an additional damping control loop could be useful to further enhance the performance of the improved system in order to cover the full range of operation. Fig. 12(a) shows the root locus of the system modes with the 2DOF controller with K_d selected as 0.001 at the wind speed of 6 m/s and the compensation level of 60%. It can be seen that the K_{ssr} decreases from 990 to 53.4 (referring to Fig. 4) with achieving the 5% damping ratio, implying a feasible solution of stabilizing the system in severe-case scenarios. Meanwhile, at the high wind speed, the damping factor of the SSR mode might be degraded as the analysis disclosed previously. It should be addressed that the degradation of the SSR mode damping may cause the instability due to integral impacts from other control parameters of the RSC

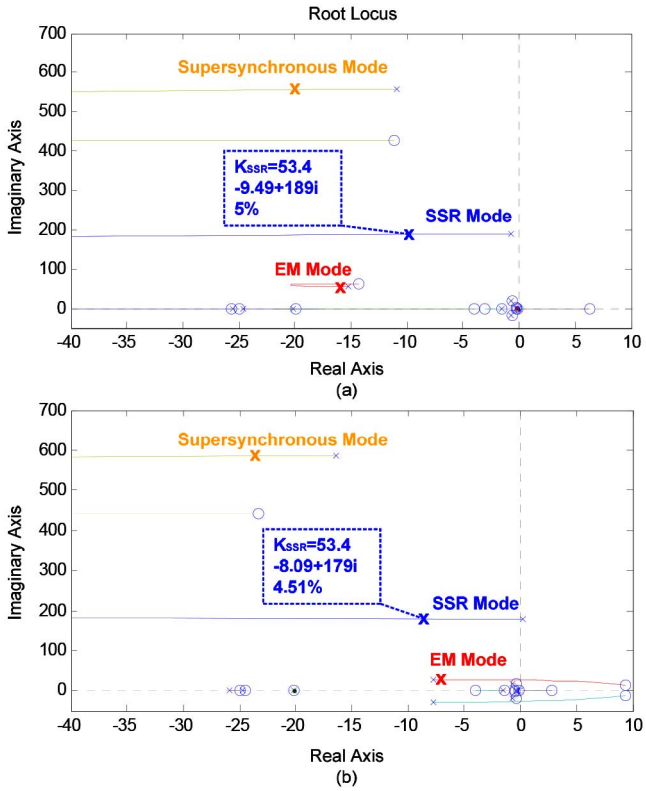

Fig. 12. Root locus of the system modes in respect to the varying K_{SSR} with the damping signal selected as the series capacitor voltage v_c and the K_d as 0.001 (Complete Model): (a) 60% compensation, 6 m/s wind speed; (b) 60% compensation, 11 m/s wind speed.

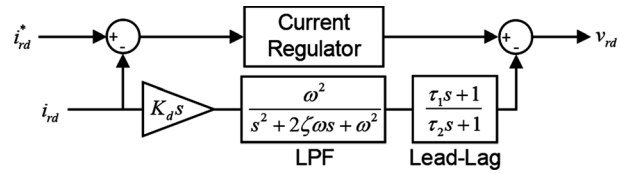

Fig. 13. Modified 2DOF derivative controller.

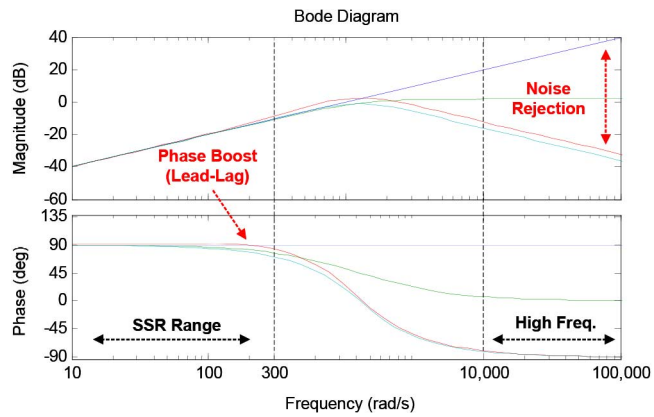

Fig. 14. Bode diagram of different types of derivative controller. (Blue: $K_d s$, Green: $K_d s/(K_d s/N+1)$, Light Blue: $K_d \omega^2 s/(s^2+2\zeta\omega s+\omega^2)$, Red: Proposed modified derivative controller.)

and GSC (e.g., RSC's current/torque loop gains). Fortunately, this can also be resolved by adding the additional damping control loop, which shifts the SSR mode back to the LHP, shown in Fig. 12(b). The derivative action sacrifices the SSR damping in high wind speeds; however, the system stability at low wind speed and high compensation is significantly improved. This means that the proposed combined control strategy not only reduces the loading (K_{ssr} decreases significantly) of the GSC in low wind speeds but also guarantees satisfactory damping performance in high wind speeds so that full-range operation can be covered.

D. Implementation of the Derivative Controller

In DFIGs, the RSC is a power electronic converter that behaves like a VSC. The switching harmonics are filtered through the inductance and resistance of the rotor circuit. When the derivative term is applied, the high switching noises may affect the controller action since the output of the derivative term is proportional to the input frequency. In practical applications, the derivative term is usually combined with a first-order low pass filter and thus becomes $K_d s/(K_d s/N+1)$. However, this can only limit the maximum gain to N. In order to achieve better damping performance and high frequency noise attenuation, a modified derivative controller is proposed and shown in Fig. 13, comprising an additional 2nd order filter and a lead-lag compensator [21]. The Bode diagram of different types of derivative controller is shown in Fig. 14, indicating that the second-order filter has better high frequency rejection but less phase shift in lower frequency compared to the first order filter. Thus, the lead-lag compensator is necessarily to be utilized to boost up the phase shift to around 90 degree in the region of interest (SSR region). The selection of the parameters of the 2nd order filter is based on cutting off the high frequency components (200 Hz in this paper) with the damping factor selected as 0.707. Also, the lead-lad compensator is tuned to compensate the phase loss at lower frequency by selecting a zero of $225(1/\tau_1)$ and a pole of $350(1/\tau_2)$ so that the maximum phase compensation occurs within this range.

V. Time-Domain Analysis

The proposed SSR mitigation strategy has been discussed through the eigenvalue analysis, root locus method, and impedance-based criteria. In order to verify its effectiveness, time-domain simulations are required to reflect the actual dynamic behavior during disturbances. The simulation scenarios are divided into three sets: 1) no mitigation strategy; 2) with only the damping control loop; 3) with the proposed combined 2DOF and damping control. The capacitor voltage is estimated through the proposed algorithm by assuming the maximum compensation level of 60%. All the scenarios are tested under different wind speeds and compensation levels with K_{d} and K_{ssr} selected as 0.001 and 53.4. Also, the modified derivative controller is adopted based on the parameters shown in the previous section.

A. Performance at Different Levels of Series Compensation

Fig. 15 shows the dynamic response of the system at 6 m/s wind speed and 60% compensation level. The compensation level changes at 0.2 s from 25% to 60%. It should be mentioned that only the scenario 3 is shown in this figure as in other two scenarios the system becomes unstable (referring to

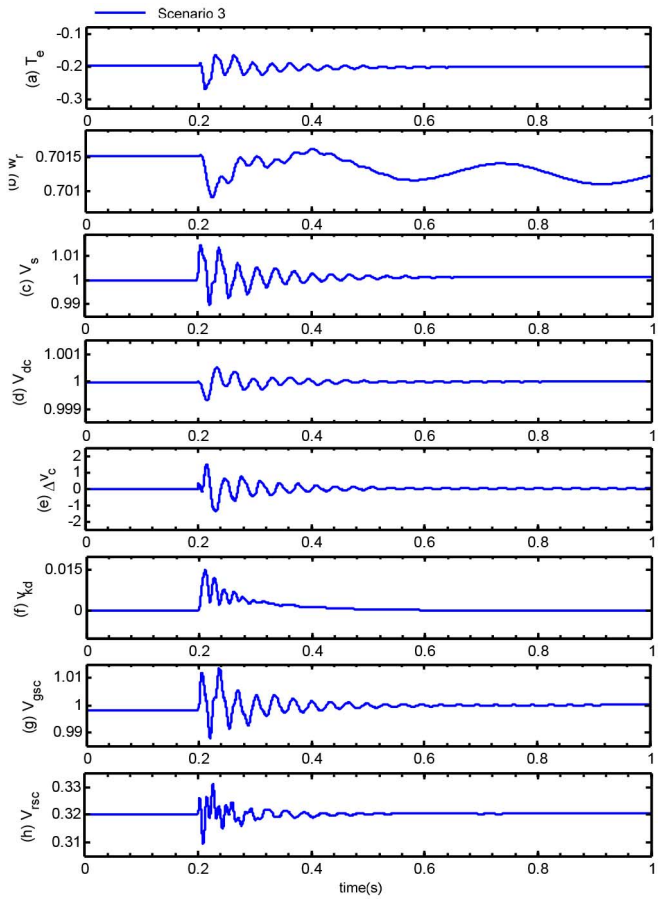

Fig. 15. Dynamic response of the system (60% compensation, 6 m/s). (a) Electrical torque. (b) Rotor speed. (c) Stator voltage. (d) DC-Link voltage. (e) Damping controller output. (f) Derivative controller output magnitude. (g) GSC output voltage. (h) RSC output voltage (pu).

Table III). With the proposed control strategy the system is stabilized and resumes its normal operation. The damping controller output based on the estimated capacitor voltage is presented in Fig. 15(e). Since the magnitude of the Δ_{v_c} is larger than the nominal voltage reference, during the transients GSC is mostly generating damping voltage to stabilize the system with the voltage error signal fed to and scaled down by the proportional gain, $K_{p5} = 0.01$, of the GSC's voltage controller. After the disturbance, Δ_{v_c} resumes to zero and does not affect the voltage controller of the GSC. The GSC's terminal output is shown in Fig. 15(g).

The result in the case with 6 m/s wind speed and 40% compensation level is shown in Fig. 16. The damping of the system is improved significantly by the proposed control strategy; the performance of the proposed combined control strategy is assisting in stabilizing the system, while other two scenarios are not stable and now shown in the figure. Fig. 17 shows the simulation results at the wind speed of 9 m/s based on compensation levels of 60%. The proposed control strategy demonstrates significant improvement against the SSR compared to other two scenarios. It can be also observed that the sustained oscillation occurs without any damping control strategy. For the high wind speed condition, the 11 m/s wind speed cases with 60% compensation levels are shown in Fig. 18. Although the effectiveness of

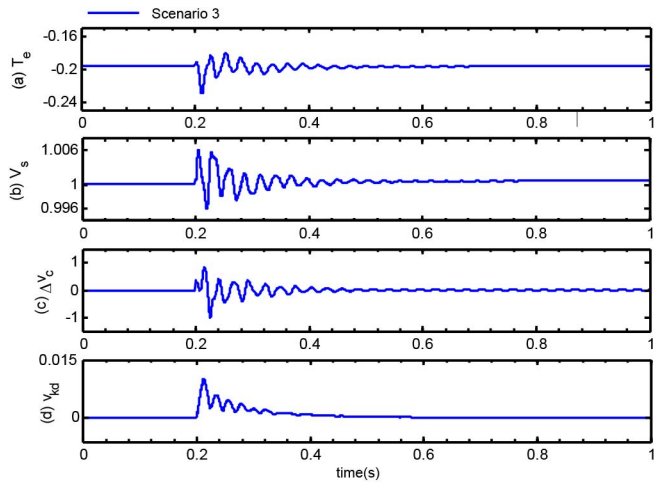

Fig. 16. Dynamic response of the system (40% compensation, 6 m/s). (a) Electrical torque. (b) Stator voltage. (c) Damping controller output. (d) Derivative controller output magnitude (pu).

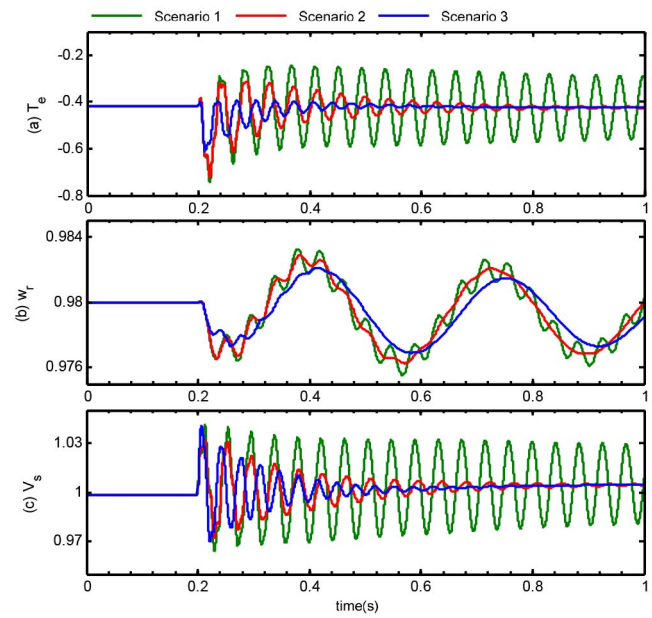

Fig. 17. Dynamic response of the system (60% compensation, 9 m/s). (a) Electrical torque. (b) Rotor speed. (c) Stator voltage (pu).

proposed 2DOF controller is compromised as discussed previously, the overall performance with the combined strategy does not deviate much from the scenario 2.

The time-domain analysis reflects the system actual response during the transient stage. The nonlinearity that cannot be extracted precisely is then examined through the time-domain simulation. The comparison is further evaluated via the dynamic responses based on the fourth scenario (with only the 2DOF controller) at the compensation level of 60% and different wind speeds, shown in Fig. 19. Notably, the small positive value of the SSR mode at the 11m/s case (blue) is observed from the poorly damped signals of T_e. This also demonstrates the accuracy of the eigenvalue analysis, indicating that in high wind speeds the 2DOF requires the assistance from the damping controller to damp the system oscillation.

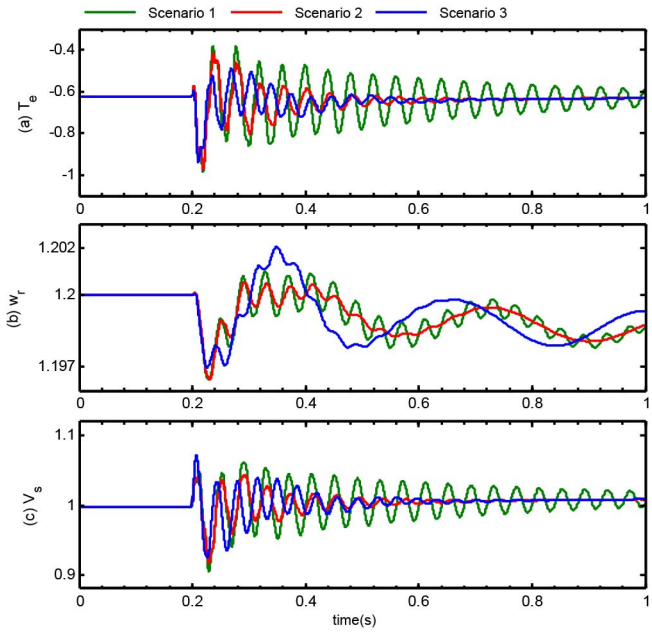

Fig. 18. Dynamic response of the system (60% compensation, 11 m/s). (a) Electrical torque. (b) Rotor speed. (c) Stator voltage (pu).

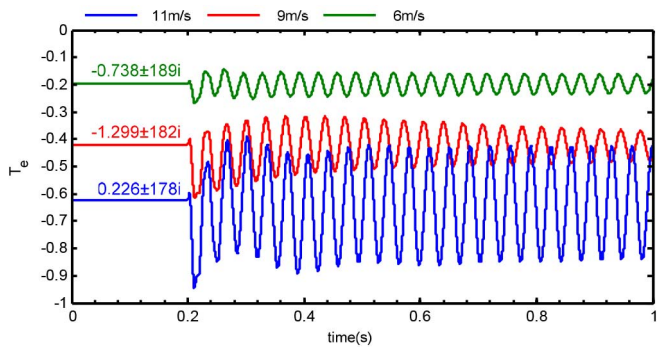

Fig. 19. Dynamic response of the system with only the 2DOF derivative control at different wind speeds (60% compensation, pu).

B. *Discussion of Fault Ride-Through Capability*

The recent grid codes [22] specifies that large wind farms are to stay connected to the grids when faults occur, since the disconnection may further degrade voltage restoration during and after fault conditions. Fault ride-through (FRT) capability is essential for grid-connected DFIG wind generation to maintain continued operation against severe grid voltage disturbances. Conventional FRT schemes have been proposed by many literatures to protect the DFIG system from overcurrent such as crowbar, DC-choppers, rotor/stator braking resistors, and series braking resistors. In addition, series voltage compensation topologies using power electronic converters show satisfactory results again severe faulty condition. There are many FRT options possible to incorporate with the proposed SSR controller. To demonstrate the performance of the proposed SSR mitigation strategy against faults, a convenient FRT scheme with single-step series braking resistors connected to the DFIG system terminal is utilized to investigate the dynamic response during and after the fault, shown in Fig. 20. The braking resistors are to be

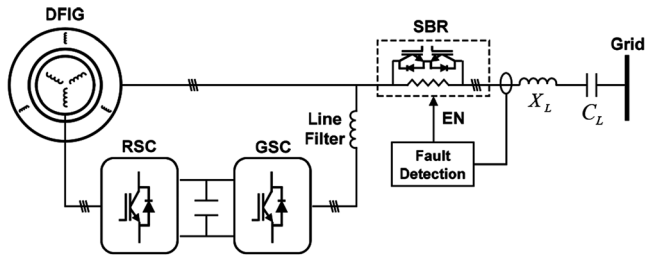

Fig. 20. Circuit diagram of the DFIG system connected to the series braking resistors and the series-compensated network.

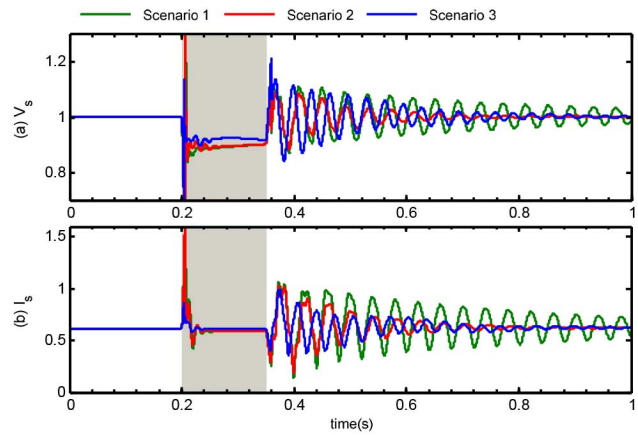

Fig. 21. Simulation results of the system during 90% there-phase-to-ground voltage dips for 150 ms (60% compensation, 11 m/s). (a) Stator voltage. (b) Stator current (pu).

engaged by turning off the by-pass IGBT switches based on the measured grid voltage. It should be addressed that the case study is simply to show that the proposed SSR mitigation strategy can be integrated into the FRT scheme. Different FRT schemes may need further modifications or investigations according to the grid code requirement and the FRT configurations.

The performance of the proposed control scheme associated with the FRT scheme is shown in Figs. 21 and 22, where a 90% three-phase-to-ground fault occurs at 0.2 s for 150 ms. During the fault, the damping controller does not play a significant role since the SSR mode disappears quickly due to insertion of high series braking resistance (1.1 pu). However, during fault recovery stage the SSR component becomes very large and affects the system stability. With the proposed scheme, the results show that post-fault behavior is significant improved in the 9m/s case; without, significant oscillation is induced at SSR frequency. Furthermore, the case study without engaging the braking resistor at low wind speed of 6 m/s is shown in Fig. 23 to demonstrate the effectiveness of the proposed scheme. It should be mentioned that the large output of the derivative controller in Fig. 23(e) is actually constrained by the DC-link voltage, which determines the maximum RSC output voltage, shown in Fig. 23(g) (the nominal maximum value is around 0.37 and the model under study neglects the stator/rotor turn ratio). From the figure, other state variables are within the acceptable range and the system is stabilized via the proposed SSR mitigation strategy.

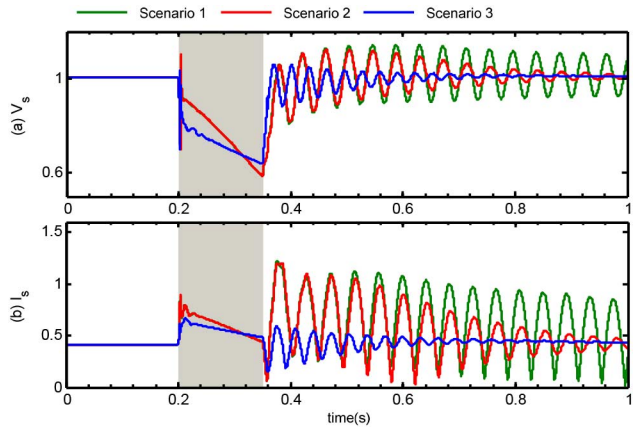

Fig. 22. Simulation results of the system during 90% there-phase-to-ground voltage dips for 150 ms (60% compensation, 9 m/s). (a) Stator voltage. (b) Stator current (pu).

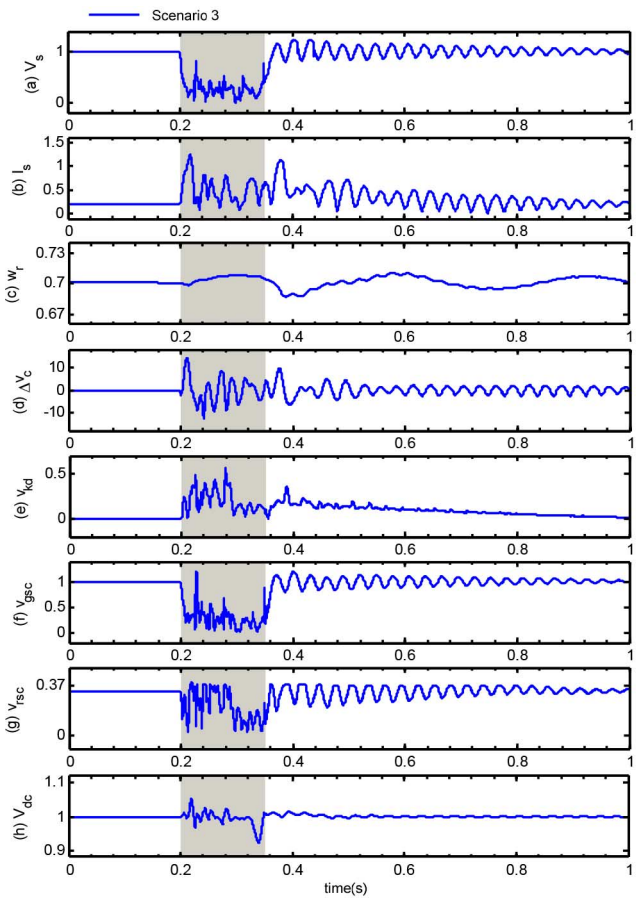

Fig. 23. Simulation results of the system during 90% there-phase-to-ground voltage dips for 150 ms (60% compensation, 6 m/s). (a) Stator voltage. (b) Stator current. (c) Rotor speed. (d) Damping controller output. (e) Derivative controller output. (f) GSC's terminal output. (g) RSC's terminal output. (h) DC-link voltage (pu).

VI. Conclusion

This paper focuses on analyzing the harmful SSR behavior of DFIG based wind farms, which is caused by IGE. Thus, the mitigation of SSR and the enhancement of the system damping are important in maintaining the entire power system stability. A reliable way of investigating the system and designing an effective control strategy against SSR is deployed using eigenvalue analysis. The proposed 2DOF control strategy improves the SSR handling capability of the system. With an additional damping control loop, the system can be secured in various compensation levels and wind speeds, especially at low wind speeds and high compensation levels. Time-domain simulation results are carried out to show the performance improvement of the proposed control strategy based on the improved capacitor voltage estimation method, and further to verify the eigenvalue analysis. Finally, the function of FRT is also demonstrated in this study showing the effectiveness of the proposed controller during faulty conditions.

References

[1] "First benchmark model for computer simulation of subsynchronous resonance," *IEEE Trans. Power App. Syst.*, vol. PAS-96, pp. 1565–1572, 1977.

[2] X. Xiaorong, G. Xijiu, and H. Yingduo, "Mitigation of multimodal SSR using SEDC in the Shangdu series-compensated power system," *IEEE Trans. Power Syst.*, vol. 26, pp. 384–391, 2011.

[3] N. Johansson, L. Angquist, and H. P. Nee, "A comparison of different frequency scanning methods for study of subsynchronous resonance," *IEEE Trans. Power Syst.*, vol. 26, pp. 356–363, 2011.

[4] P. M. Anderson, B. L. Agrawal, and J. E. Van Ness, *Subsynchronous Resonance in Power Systems*. Piscataway, NJ, USA: IEEE Press, 1999.

[5] D. N. Walker, C. E. J. Bowler, R. L. Jackson, and D. A. Hodges, "Results of subsynchronous resonance test at Mohave," *IEEE Trans. Power App. Syst.*, vol. PAS-94, pp. 1878–1889, 1975.

[6] A. A. Fouad and K. T. Khu, "Damping of torsional oscillations in power systems with series-compensated lines," *IEEE Trans. Power App. Syst.*, vol. PAS-97, pp. 744–753, 1978.

[7] M. Bongiorno, J. Svensson, and L. Angquist, "Single-phase VSC based SSSC for subsynchronous resonance damping," *IEEE Trans. Power Del.*, vol. 23, pp. 1544–1552, 2008.

[8] ABB, "Series compensation boosting transmission capacity," Reference case study, Dec. 2010.

[9] M. S. El-Moursi, B. Bak-Jensen, and M. H. Abdel-Rahman, "Novel STATCOM controller for mitigating SSR and damping power system oscillations in a series compensated wind park," *IEEE Trans. Power Electron.*, vol. 25, pp. 429–441, 2010.

[10] A. Ostadi, A. Yazdani, and R. K. Varma, "Modeling and stability analysis of a DFIG-based wind-power generator interfaced with a series-compensated line," *IEEE Trans. Power Del.*, vol. 24, pp. 1504–1514, 2009.

[11] R. K. Varma, S. Auddy, and Y. Semsedini, "Mitigation of subsynchronous resonance in a series-compensated wind farm using FACTS controllers," *IEEE Trans. Power Del.*, vol. 23, pp. 1645–1654, 2008.

[12] L. Fan, R. Kavasseri, Z. L. Miao, and C. Zhu, "Modeling of DFIG-based wind farms for SSR analysis," *IEEE Trans. Power Del.*, vol. 25, pp. 2073–2082, 2010.

[13] K. R. Padiyar and N. Prabhu, "Design and performance evaluation of subsynchronous damping controller with STATCOM," *IEEE Trans. Power Del.*, vol. 21, pp. 1398–1405, 2006.

[14] F. Al-Jowder, "Improvement of synchronizing power and damping power by means of SSSC and STATCOM—a comparative study," *Int. J. Elect. Power Syst. Res.*, vol. 77, pp. 1112–1117, 2007.

[15] L. Fan and Z. Miao, "Mitigating SSR using DFIG-based wind generation," *IEEE Trans. Sustain. Energy*, vol. 3, pp. 349–358, 2012.

[16] N. W. Miller, J. J. Sanchez-Gasca, W. W. Price, and R. W. Delmerico, "Dynamic modeling of GE 1.5 and 3.6 MW wind turbine-generators for stability simulations," in *Proc. 2003 IEEE Power Eng. Soc. General Meeting*, 2003, vol. 3, pp. 1977–1983.

[17] F. Mei and B. Pal, "Modal analysis of grid-connected doubly fed induction generators," *IEEE Trans. Energy Convers.*, vol. 22, pp. 728–736, 2007.

[18] M. Araki and H. Taguchi, "Two-degree-of-freedom PID controllers," *Int. J. Control Autom. Syst.*, vol. 1, pp. 401–411, 2003.

[19] S. Jian, "Impedance-based stability criterion for grid-connected inverters," *IEEE Trans. Power Electron.*, vol. 26, pp. 3075–3078, 2011.

[20] L. Fan and Z. Miao, "Nyquist-stability-criterion-based SSR explanation for type-3 wind generators," *IEEE Trans. Energy Convers.*, vol. 27, pp. 807–809, 2012.
[21] *Practical PID Control*. New York, NY, USA: Springer, 2006.
[22] M. Tsili and S. Papathanassiou, "A review of grid code technical requirements for wind farms," *IET Renew. Power Gener.*, vol. 3, pp. 308–332, 2009.

Po-Hsu Huang was born in Taiwan in 1985. He received the B.Sc. degree from National Cheng-Kung University, Tainan, Taiwan, and the M.Sc. degree from National Taiwan University, Taipei, Taiwan, in 2007 and 2009, respectively, both in electrical engineering.

He is currently working as a research engineer in the Department of Electrical Power Engineering, Masdar Institute of Science and Technology, Abu Dhabi, United Arab Emirates. His current interests include DC/AC microgrids, power electronics, wind power generation, linear/nonlinear system dynamics, power system stability, and control.

Mohamed Shawky El Moursi (M'12) received the B.Sc. and M.Sc. degrees from Mansoura University, Mansoura, Egypt, in 1997 and 2002, respectively, and the Ph.D. degree from the University of New Brunswick (UNB), Fredericton, NB, Canada, in 2005, all in electrical engineering.

He was a Research and Teaching Assistant in the Department of Electrical and Computer Engineering, UNB, from 2002 to 2005. He joined McGill University as a Postdoctoral Fellow with the Power Electronics Group. He joined Vestas Wind Systems, Arhus, Denmark, in the Technology R&D with the Wind Power Plant Group. He was with TRANSCO, UAE, as a Senior Study and Planning Engineer and seconded as Faculty member in the Faculty of Engineering, Mansoura University. He is currently an Associate Professor in the Electrical Engineering and Computer Science Department at Masdar Institute of Science and Technology and a Visiting Professor at Massachusetts Institute of Technology, Cambridge, MA, USA. His research interests include power system, power electronics, FACTS technologies, system control, wind turbine modeling, wind energy integration, and interconnections.

Weidong Xiao (S'04–M'07–SM'13) received the Master's and the Ph.D. degrees in electrical engineering from the University of British Columbia, Vancouver, BC, Canada, in 2003 and 2007, respectively.

He is an Associate Professor with the Department of Electrical Engineering and Computer Science (EECS), Masdar Institute of Science and Technology, Abu Dhabi, United Arab Emirates. In 2010, he was a Visiting Scholar with the Massachusetts Institute of Technology (MIT), Cambridge, MA, USA, where he worked on the power interfaces for PV power systems. Prior to the academic career, he worked as a R&D engineering manager with MSR Innovations Inc., Burnaby, BC, Canada, focusing on integration, research, optimization, and design of photovoltaic power systems. His research interest includes photovoltaic power systems, power electronics, dynamic systems and control, and industry applications.

Dr. Xiao is presently an Associate Editor of the IEEE TRANSACTIONS ON INDUSTRIAL ELECTRONICS.

James L. Kirtley, Jr. (F'91) received the Ph.D. degree in electrical engineering from the Massachusetts Institute of Technology (MIT), Cambridge, MA, USA, in 1971.

He has been a member of the faculty of the Department of Electrical Engineering and Computer Science, MIT, since 1971, where he is currently Professor of Electrical Engineering. He was also an Electrical Engineer with the Large Steam Turbine Generator at General Electric, General Manager and Chief Scientist with SatCon Technology Corporation, and was Gastdozent at the Swiss Federal Institute of Technology. He is a specialist in electric machinery and electric power systems. He is a member of the Editorial Board of the journal *Electric Power Components and Systems*.

Prof. Kirtley is a Registered Professional Engineer in Massachusetts. He is a member of the U.S. National Academy of Engineering. He was awarded the Nikola Tesla Prize in 2002 and the IEEE Third Millennium medal. He was Editor-in-Chief of the IEEE TRANSACTIONS ON ENERGY CONVERSION from 1998 to 2006 and continues to serve as an Editor for that journal.